GEOPHYSICS, VOL. 68, NO. 3 (MAY-JUNE 2003); P. 1091–1102, 15 FIGS.
10.1190/1.1581081

Adaptive decomposition of multicomponent ocean-bottom seismic data into downgoing and upgoing P- and S-waves

K. M. Schalkwijk*, C. P. A. Wapenaar‡, and D. J. Verschuur*

ABSTRACT

With wavefield decomposition, the recorded wavefield at a certain depth level can be separated into upgoing and downgoing wavefields as well as into P- and S-waves. The medium parameters at the considered depth level (e.g., just below the ocean-bottom) need to be known in order to be able to do a decomposition. In general, these parameters are unknown and, in addition, measurement-related issues, such as geophone coupling and crosstalk between the different components, need to be dealt with. In order to apply decomposition to field data, an adaptive five-stage decomposition scheme was developed in which these issues are addressed.

In this study, the adaptive decomposition scheme is tested on a data example with a relatively shallow water depth (~120 m), consisting recordings from of a full line of ocean-bottom receivers. Although some of the individual stages in the decomposition scheme are more difficult to apply because of stronger interference between events compared to data acquired over deeper water, the end result is satisfying. Also, a good decomposition result is obtained for the S-waves. The extension of the decomposition scheme to a complete line of ocean-bottom cable data consists of a repeated application of the procedure for each receiver. The resulting decomposed upgoing P- and S-wavefields are processed, yielding poststack time migrated images of the subsurface. Comparison with the images obtained from the original (i.e., not decomposed) measurements shows that wavefield decomposition just below the ocean bottom leads to a strong attenuation of multiply reflected events at the sea surface and better event definition in both P- and S-wave sections. Other decomposition effects like improved angle-dependent amplitudes cannot be evaluated in this way.

INTRODUCTION

The aim of decomposition of multicomponent ocean-bottom seismic data is to separate the measurements into their downgoing and upgoing P- and S-wave constituents. Wavefield decomposition can be used as a first step in the data processing sequence for multicomponent seismic data. Data processing of the separated waves is easier than full vector wavefield processing and is less sensitive to errors in the macrovelocity model of the subsurface.

The decomposition procedure in essence combines the pressure and horizontal and vertical particle velocity components after application of the appropriate decomposition operator to each of these components. In order to calculate the elastic decomposition operators, the medium parameters just below the receiver level need to be known. This indicates why application of decomposition to field data is not straightforward: the medium parameters are generally unknown and, due to measurement imperfections (different coupling, impulse response, etc.), the components need to be calibrated to each other before they can be combined.

To apply decomposition to field data, without having any a priori information, it is therefore necessary to formulate a more practical decomposition procedure. The decomposition equations can be simplified by splitting them into a part that separates downgoing and upgoing wavefields and a part that separates the P- and S-waves. Furthermore, a good decomposition result leaves no downgoing waves in the upgoing wavefield and vice versa. The best possible decomposition result can therefore be obtained by formulating an optimization problem on these criteria. The unknown parameters are then contained in the resulting optimization filter. To obtain values for the medium parameters, this filter has to be inverted. This

Manuscript received by the Editor May 15, 2000; revised manuscript received July 23, 2002.
*Delft University of Technology, Department of Applied Physics, P.O. Box 5046, 2600 GA Delft, Netherlands. E-mail: karin@akst.tn.tudelft.nl; d.j.verschuur@ctg.tudelft.nl.
‡Delft University of Technology, Department of Applied Earth Sciences, P.O.Box 5028, 2600 GA Delft, Netherlands. E-mail: c.p.a.wapenaar@ctg.tudelft.nl.

decomposition procedure has been introduced and demonstrated on one deep-water field-data common-receiver gather in Schalkwijk et al. (1999).

To further test the possibilities and limitations of the adaptive decomposition scheme, in this study a shallow-water data example is considered. As this example contains high-quality ocean-bottom cable (OBC) recordings for a full line of receivers, aspects such as the extension of decomposition to larger data sets (including the estimation of the subbottom medium parameters) and the effect of wavefield decomposition on the quality of the seismic image can be investigated.

WAVEFIELD DECOMPOSITION

In the case of a decomposition at the ocean bottom, there is the choice of performing a decomposition just above the bottom (acoustic decomposition) or just below the bottom (elastic decomposition). In the former case, the downgoing and upgoing pressure wavefields in the water layer are obtained; the latter case results in the downgoing and upgoing P- and S-waves just below the receiver level. The composition and decomposition equations [equations (1) and (2) below] give the relations between the two-way wavefield vectors (in terms of the total particle velocity and traction) and one-way wavefield vectors (acoustically in terms of downgoing and upgoing pressure wavefields, elastically in terms of potentials for downgoing and upgoing P- and S-waves).

Relations between two-way and one-way wavefields

For laterally invariant media, derivations of the decomposition equations by eigenvalue decomposition of the elastic wave equation have been given in various publications (Frasier, 1970; Aki and Richards, 1980; Kennett, 1983; Ursin, 1983). When written in the ray parameter-frequency (p,ω) domain, the composition/decomposition equations for each frequency component are given by

$$\begin{pmatrix} -\tilde{\boldsymbol{\tau}}_z(z) \\ \tilde{\mathbf{V}}(z) \end{pmatrix} = \begin{pmatrix} \tilde{\mathbf{L}}_1^+(z) & \tilde{\mathbf{L}}_1^-(z) \\ \tilde{\mathbf{L}}_2^+(z) & \tilde{\mathbf{L}}_2^-(z) \end{pmatrix} \begin{pmatrix} \tilde{\mathbf{D}}^+(z) \\ \tilde{\mathbf{D}}^-(z) \end{pmatrix} \qquad (1)$$

and

$$\begin{pmatrix} \tilde{\mathbf{D}}^+(z) \\ \tilde{\mathbf{D}}^-(z) \end{pmatrix} = \begin{pmatrix} \tilde{\mathbf{N}}_1^+(z) & \tilde{\mathbf{N}}_2^+(z) \\ \tilde{\mathbf{N}}_1^-(z) & \tilde{\mathbf{N}}_2^-(z) \end{pmatrix} \begin{pmatrix} -\tilde{\boldsymbol{\tau}}_z(z) \\ \tilde{\mathbf{V}}(z) \end{pmatrix}, \qquad (2)$$

respectively. Note that only the depth dependency has been written explicitly (denoted by z; the z-axis is pointing downward). Hence, $\tilde{\mathbf{V}}(z)$ stands for $\tilde{\mathbf{V}}(p,z,\omega)$, etc. The composition and decomposition operators $\tilde{\mathbf{L}}$ and $\tilde{\mathbf{N}}$ are given in Schalkwijk et al. (1999), and derived in Schalkwijk (2001). The vector $[(\tilde{\mathbf{D}}^+)^T \ (\tilde{\mathbf{D}}^-)^T]^T$ contains the monochromatic one-way wavefields (downgoing and upgoing P- and S-wavefields). The vector $[-\tilde{\boldsymbol{\tau}}_z^T \ \tilde{\mathbf{V}}^T]^T$ contains the two-way wavefields in terms of stresses and particle velocities. At the ocean bottom (at depth level z_1), the stress vector reduces to $\tilde{\boldsymbol{\tau}}_z(z_1) = (0 \ -\tilde{P}(z_1))^T$, where $\tilde{P}$ is the acoustic pressure, and the particle velocity vector to $\tilde{\mathbf{V}}(z_1) = (\tilde{V}_x(z_1) \ \tilde{V}_z(z_1))^T$ for the 2D situation. Therefore, application of 2D elastic wavefield decomposition to ocean-bottom seismic measurements [i.e., application of equation (2)] can be schematically denoted as

$$\begin{pmatrix} 0 \\ \tilde{P}(z_1) \\ \tilde{V}_x(z_1) \\ \tilde{V}_z(z_1) \end{pmatrix} \rightarrow \begin{pmatrix} \tilde{\Phi}^+(z_1) \\ \tilde{\Psi}^+(z_1) \\ \tilde{\Phi}^-(z_1) \\ \tilde{\Psi}^-(z_1) \end{pmatrix}, \qquad (3)$$

where the one-way wave vector $[(\tilde{\mathbf{D}}^+)^T \ (\tilde{\mathbf{D}}^-)^T]^T$ is written explicitly in terms of downgoing and upgoing P-wave potentials ($\Phi^\pm$) and S-wave potentials ($\Psi^\pm$). This procedure separates the downgoing and upgoing waves as well as the P- and S-waves simultaneously, provided the P- and S-velocities and density of the medium at the considered depth level are known. In equation (3) the $\tilde{V}_y$ component is not taken into account, which means we are actually assuming line-source data in a medium that is invariant in the y-direction, instead of point-source data in a 3D inhomogeneous medium. Furthermore, the medium just below the ocean bottom is assumed to be isotropic. Note that any kind of anisotropy can be present further below the ocean floor, as long as the anisotropy parameters do not vary in the y-direction. Strictly speaking, a transformation from 3D to 2D amplitudes should take place. For horizontally layered isotropic media, this transformation can be formulated exactly (see Wapenaar et al., 1992). In practice, small deviations from the horizontal layering can already lead to large artifacts in the transformed data (which can be stabilized by using common-midpoint-gathers). In the Mahogany data example (below), the amplitude has been corrected by multiplication with the square-root of time. As the decomposition is mainly sensitive to relative amplitudes, it will still work quite well, even without amplitude correction.

Because actual measurements of the pressure and particle velocity are not identical to the theoretical pressure and particle velocity in equations (1) and (2) and the medium parameters just below the ocean-bottom are unknown, a straightforward combination of pressure and particle velocity components to obtain downgoing and upgoing P- and S-waves [application of equation (2)] is not possible on field data. When applying decomposition to field data, it is more advantageous to perform the decomposition into downgoing and upgoing waves and the decomposition into P- and S-waves separately. This procedure can be schematically denoted as

$$\begin{pmatrix} \begin{pmatrix} 0 \\ \tilde{P}(z_1) \end{pmatrix} \\ \begin{pmatrix} \tilde{V}_x(z_1) \\ \tilde{V}_z(z_1) \end{pmatrix} \end{pmatrix} \rightarrow \begin{pmatrix} \begin{pmatrix} \tilde{\tau}_{xz}^+(z_1) \\ \tilde{\tau}_{zz}^+(z_1) \end{pmatrix} \\ \begin{pmatrix} \tilde{\tau}_{xz}^-(z_1) \\ \tilde{\tau}_{zz}^-(z_1) \end{pmatrix} \end{pmatrix} \rightarrow \begin{pmatrix} \begin{pmatrix} \tilde{\Phi}^+(z_1) \\ \tilde{\Psi}^+(z_1) \end{pmatrix} \\ \begin{pmatrix} \tilde{\Phi}^-(z_1) \\ \tilde{\Psi}^-(z_1) \end{pmatrix} \end{pmatrix}, \qquad (4)$$

where the downgoing and upgoing fields in the intermediate result are expressed in terms of stresses, where $\tilde{\boldsymbol{\tau}}_z^\pm(z_1) = (\tilde{\tau}_{xz}^\pm(z_1) \ \tilde{\tau}_{zz}^\pm(z_1))^T$ and $\tilde{\boldsymbol{\tau}}_z = \tilde{\boldsymbol{\tau}}_z^+ + \tilde{\boldsymbol{\tau}}_z^-$. This results in a simple form of the decomposition equations (see Schalkwijk et al., 1999), such that not all measured components have to be combined simultaneously.

The "two-step decomposition operators" can be derived from equation (1) as follows:

$$\begin{pmatrix} -\tilde{\boldsymbol{\tau}}_z^+(z_1) \\ -\tilde{\boldsymbol{\tau}}_z^-(z_1) \end{pmatrix} = \begin{pmatrix} \tilde{\mathbf{L}}_1^+(z_1) & \mathbf{O} \\ \mathbf{O} & \tilde{\mathbf{L}}_1^-(z_1) \end{pmatrix} \begin{pmatrix} \tilde{\mathbf{D}}^+(z_1) \\ \tilde{\mathbf{D}}^-(z_1) \end{pmatrix}, \quad (5)$$

or, upon substitution of equation (2);

$$\begin{pmatrix} -\tilde{\boldsymbol{\tau}}_z^+(z_1) \\ -\tilde{\boldsymbol{\tau}}_z^-(z_1) \end{pmatrix} = \begin{pmatrix} \tilde{\mathbf{M}}_1^+(z_1) & \tilde{\mathbf{M}}_2^+(z_1) \\ \tilde{\mathbf{M}}_1^-(z_1) & \tilde{\mathbf{M}}_2^-(z_1) \end{pmatrix} \begin{pmatrix} -\tilde{\boldsymbol{\tau}}_z(z_1) \\ \tilde{\mathbf{V}}(z_1) \end{pmatrix}, \quad (6)$$

where the partial decomposition operators are defined as

$$\tilde{\mathbf{M}}_1^{\pm}(z_1) = \tilde{\mathbf{L}}_1^{\pm}(z_1)\tilde{\mathbf{N}}_1^{\pm}(z_1), \quad (7)$$

$$\tilde{\mathbf{M}}_2^{\pm}(z_1) = \tilde{\mathbf{L}}_1^{\pm}(z_1)\tilde{\mathbf{N}}_2^{\pm}(z_1). \quad (8)$$

Equation (6) represents the first decomposition step in equation (4). For the second decomposition step into P- and S-waves, equation (5) is merely inverted, yielding

$$\begin{pmatrix} \tilde{\mathbf{D}}^+(z_1) \\ \tilde{\mathbf{D}}^-(z_1) \end{pmatrix} = \begin{pmatrix} \{\tilde{\mathbf{L}}_1^+(z_1)\}^{-1} & \mathbf{O} \\ \mathbf{O} & \{\tilde{\mathbf{L}}_1^-(z_1)\}^{-1} \end{pmatrix} \begin{pmatrix} -\tilde{\boldsymbol{\tau}}_z^+(z_1) \\ -\tilde{\boldsymbol{\tau}}_z^-(z_1) \end{pmatrix}. \quad (9)$$

The "two-step" formulation [equation (4)] makes it possible to apply decomposition to field data in an adaptive way, where the decomposition result is optimized by using the condition that no upgoing waves should be present in the downgoing wavefield and vice versa. An adaptive decomposition scheme with five intermediate stages was developed (Schalkwijk et al. 1999). The different stages are used for suppression of "cross-coupling," calibration of the data components, and estimation of the velocities and density just below the ocean-bottom (see Figure 1). In the last stage the downgoing and upgoing P- and S-waves are obtained.

FIELD DATA

A four-component (4C) ocean-bottom data set (courtesy of BP), acquired over Mahogany field in the Gulf of Mexico, is used here for application of the decomposition procedure. The cable with ocean-bottom receivers contained 60 receivers with a spacing of 25 m. The depth of the ocean bottom is about 120 m. The air-gun source was just below the water surface at a depth of 6 m. The interval between the shots was also

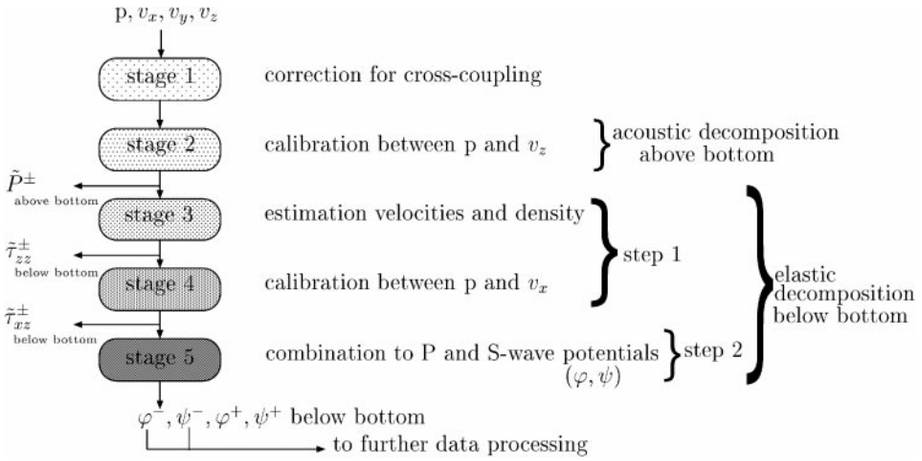

FIG. 1. Adaptive decomposition scheme for obtaining downgoing and upgoing P- and S-wave potentials from field data.

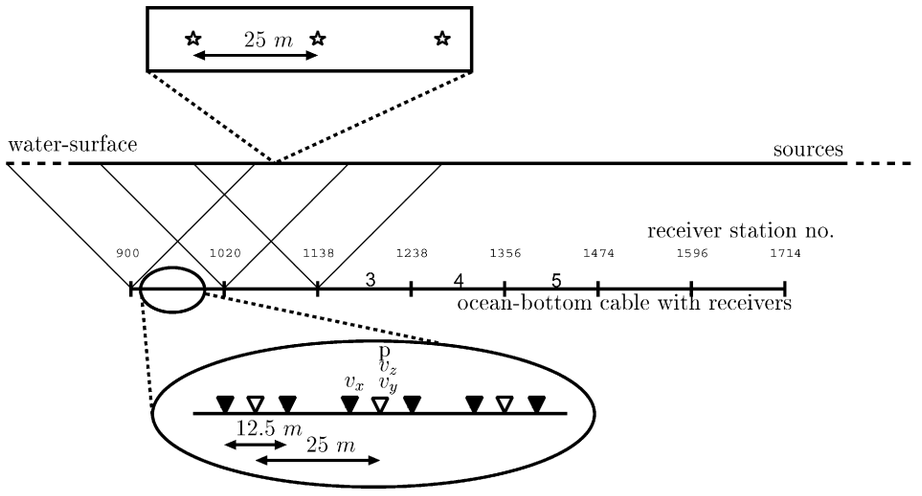

FIG. 2. Acquisition of the Mahogany ocean-bottom data.

25 m. The ocean-bottom cable was moved seven times. Each time, the source covers the cable with a maximum offset of 10 000 m. In this way, a very long receiver line (7×1500 m) is obtained. The acquisition configuration is displayed in Figure 2. The data are recorded up to 10 s with a time sampling of 4 ms. In Figures 3 and 4, the data of common-receiver gather 1321 are displayed for the four components for the total offset and time range. The pressure component in Figure 3a shows strong reverberations of the air-gun source (air-gun bubble). As the vertical partical velocity in water is proportional to the vertical derivative of the pressure, a relatively weaker low-frequency content is expected on the vertical geophone measurement. Therefore, the effect of the air-gun bubble, which has a low-frequency character, is less pronounced in Figure 3b. In addition, the vertical component displays cross-coupling with the horizontal components (the events with low moveout velocity at small offsets). The horizontal (v_x) and crossline (v_y) velocity components are displayed in Figures 4a and 4b (at the same

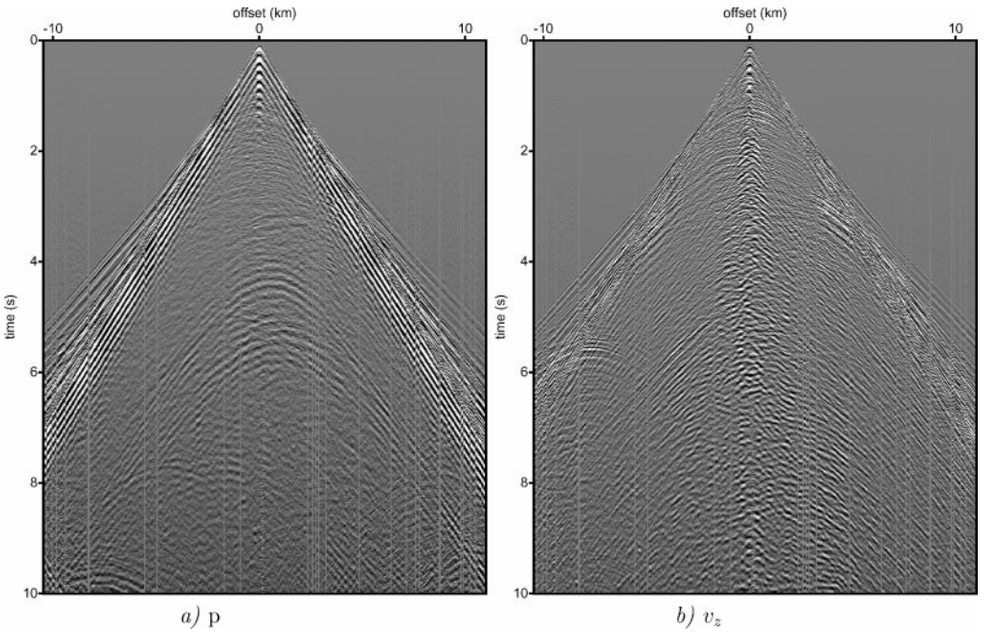

FIG. 3. Ocean-bottom measurements of one common-receiver gather (number 1321) displayed with a gain factor of $t^{1.5}$ (a) Pressure just above the bottom. (b) Vertical velocity component.

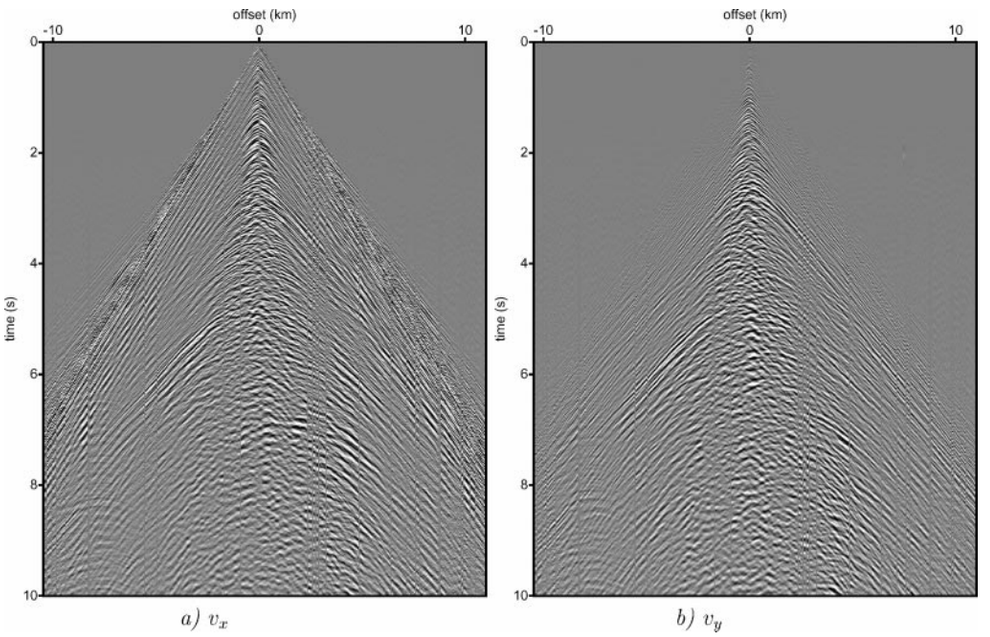

FIG. 4. Ocean-bottom measurements of one common-receiver gather (number 1321) displayed with a gain factor of $t^{1.5}$. (a) Horizontal inline velocity component. (b) Horizontal crossline velocity component.

scaling). Up to about 3 s, the energy on the v_y component is small compared to the v_x component. After that, the two components have about the same strength. This is an indication for the complex deeper structure where 3D effects come into play; for the shallower portion, the situation is more or less 2D, resulting in less energy on the v_y component compared to the v_x component. Note the similarity between the small offset low velocity moveout events in Figure 4 and the "cross-coupling" in Figure 3b. New aspects of this data example with regard to wavefield decomposition are the relatively shallow water depth and the possibility to extend and test the decomposition procedure on a full line of 2-D data. In the latter application, the determination of the subbottom medium parameters plays an important role. This, in turn, makes it also possible to compare images of the subsurface obtained with and without wavefield decomposition.

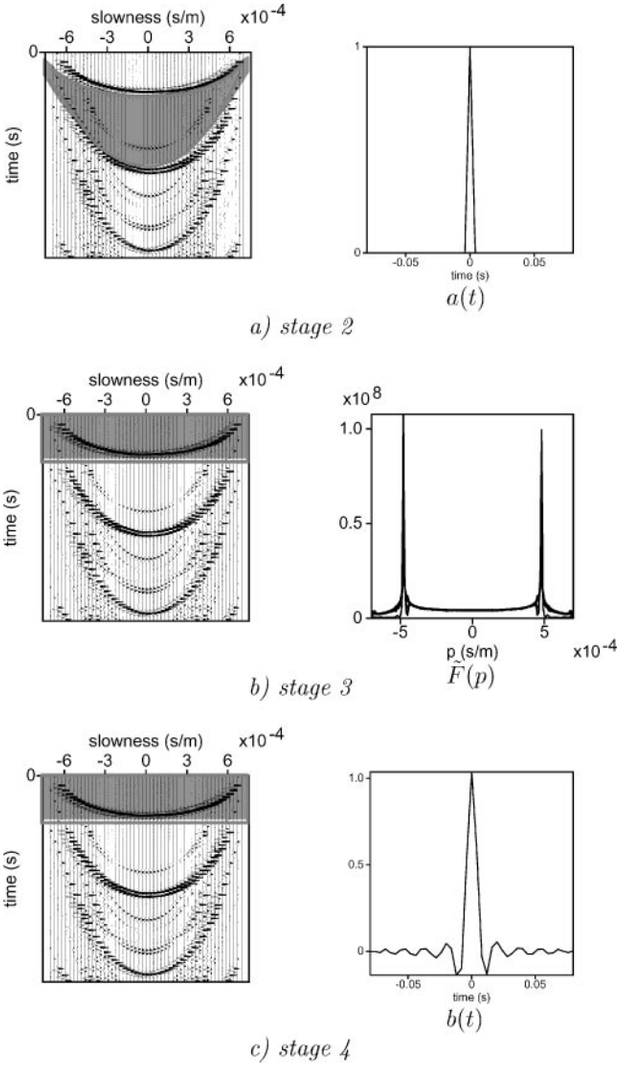

FIG. 5. The window choices (shaded areas) arising in stages 2, 3, and 4 of the adaptive decomposition scheme (shown on the pressure component in the τ, p domain) together with the obtained "optimal filters," illustrated on a synthetic data example of a horizontally layered model.

APPLICATION OF THE ADAPTIVE SCHEME TO THE MAHOGANY DATA SET

The application of the adaptive decomposition scheme is discussed by means of the Mahogany data set. In addition, window choices within the scheme are clarified using a synthetic data example with a water depth of 500 m.

Before decomposition is applied to the data, the effect of the air-gun bubble is removed by deconvolution. Because in this situation, the air-gun bubble has almost the the same periodicity as the reverberations within the water layer, special care must be taken that the water layer multiples and other interfering events are affected by the deconvolution as little as possible. To avoid aliasing in the Fourier and Radon transformations, the data are interpolated to a trace interval of 12.5 m.

The five-stage decomposition procedure is repeatedly applied to successive common-receiver gathers to decompose the full 2D dataset. At each receiver location, the medium parameters and coupling filters are estimated.

Stage 1. Corrections for cross-coupling

When the pressure and vertical velocity component in Figure 3 are compared, strong events with a low moveout velocity are observed on the velocity components that are not present on the pressure component. These events (presumably converted waves) will not be compensated for when the components are combined in the decomposition procedure and, therefore, they deteriorate the decomposition result if they are not removed. In Schalkwijk et al. (1999), it was proposed to remove the cross-coupling by optimally subtracting the horizontal velocity components from the vertical component. This procedure did not remove cross-coupling well in this case. The minimum energy criterion used in the subtraction was not applicable due to the interference of the cross-coupling with other events.

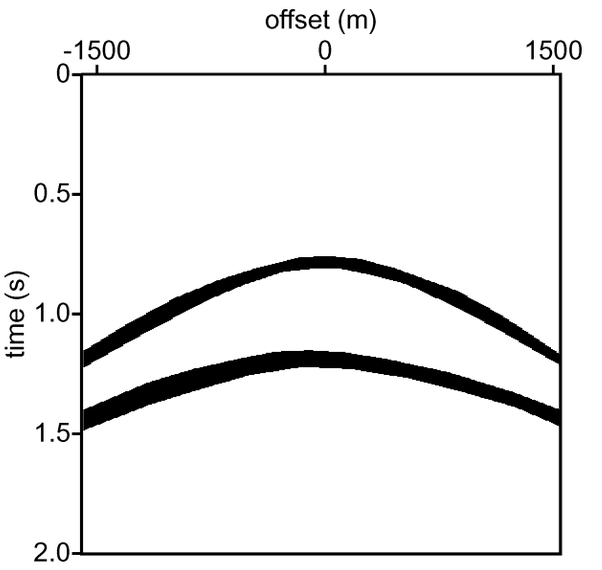

FIG. 6. Two windows over primaries used in stage 2 of the adaptive decomposition scheme, for application to the full receiver line (Mahogany data).

Stage 2. Acoustic decomposition above the ocean-bottom

In stage 2, the acoustic decomposition above the ocean bottom is used to determine a calibration filter $A(\omega)$ between the pressure and vertical velocity component. Modifying equation (2) for acoustic waves, using the appropriate expressions for $\tilde{\mathbf{N}}_1^{\pm}$ and $\tilde{\mathbf{N}}_2^{\pm}$ (Schalkwijk et al., 1999), gives in the p, ω-domain

$$\tilde{P}^{\pm} = \frac{1}{2}\tilde{P} \pm A(\omega)\frac{\varrho_0}{2q_0}\tilde{V}_z, \tag{10}$$

where ϱ_0 and q_0 are the density and vertical slowness of the water layer. The acoustic decomposition operators are known (as they depend solely on the velocity and density of the water), leaving $A(\omega)$ as the only unknown factor. The calibration filter $A(\omega)$ is determined by minimizing the energy of the primary reflections in the decomposed downgoing wavefield (in a good decomposition result the downgoing wavefield above the bottom, $\tilde{P}^{+}$, should contain no primary reflections). Therefore, in stage 2 of the adaptive decomposition scheme, a window must be found that contains mostly primary energy in the data before decomposition. Choosing the window to lie between the direct arrival and the first multiple, as is shown in Figure 5a (together with the time-domain version $a(t)$ of the calibration filter that was obtained by minimizing the energy within this window), has the advantage that the window does not change for different receiver gathers. This window choice is not possible for the Mahogany data because of the shallow water depth. Therefore, a more specific primary window had to be chosen. However, then the window is not necessarily constant over the line. Because it is too time-consuming to pick a different window for each receiver gather, a combined window covering several primary events was used (Figure 6). In this way, a constant window could still be used over the whole line.

Stage 3. Elastic decomposition into $\tau_{zz}^{\pm}$ just below the bottom

The elastic decomposition below the bottom into downgoing and upgoing normal stress fields, again uses the pressure and vertical velocity components. The expression for the downgoing and upgoing normal stress fields follows by substituting the expressions for $\tilde{\mathbf{M}}_1^{\pm}$ and $\tilde{\mathbf{M}}_2^{\pm}$ into equation (6), yielding

$$-\tilde{\boldsymbol{\tau}}_{zz}^{\pm} = \frac{1}{2}\tilde{P} \pm A(\omega)\frac{\varrho_1\beta_1}{2q_{P,1}}\tilde{V}_z, \tag{11}$$

where ϱ_1 and $q_{P,1}$ are the density and vertical P-wave slowness of the medium just below the bottom, and β_1 contains the P- and S-velocities.

The calibration filter $A(\omega)$ is already known from stage 2. This time the unknown factor is the operator in front of the $\tilde{V}_z$ component, as it depends on the (unknown) medium parameters just below the bottom. To find the operator, the expression is replaced by a general ray-parameter dependent filter $\tilde{F}(p)$:

$$-\tilde{\boldsymbol{\tau}}_{zz}^{\pm} = \frac{1}{2}\tilde{P} \pm A(\omega)\tilde{F}(p)\tilde{V}_z. \tag{12}$$

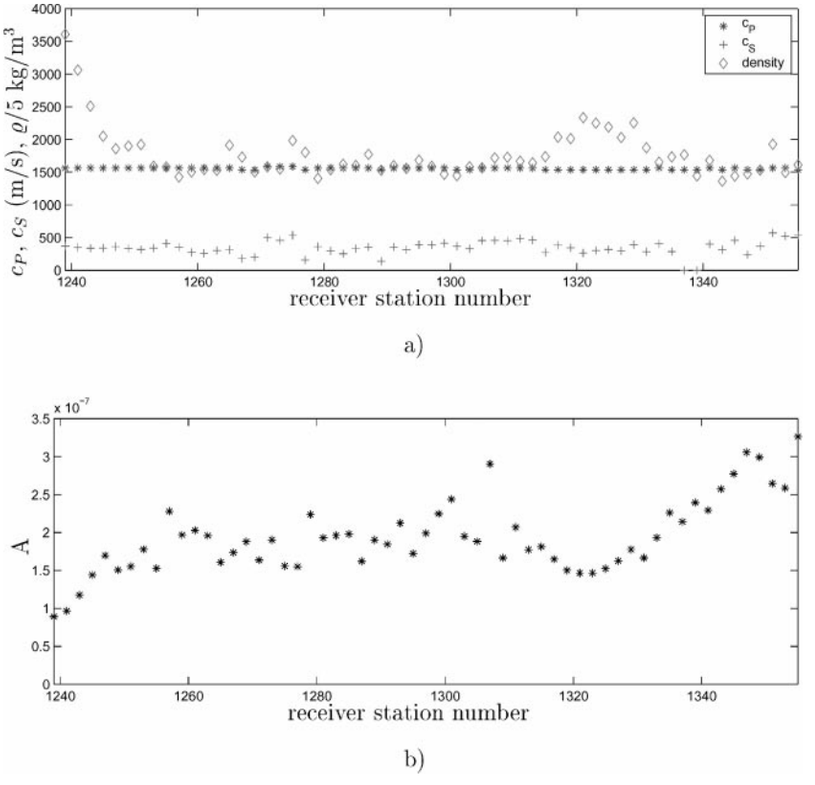

FIG. 7. (a) Inversion results for the medium parameters just below the ocean-bottom for line 4 displayed as a function of receiver station number. Diamonds denote the density estimates, stars the c_P estimates, and plusses the c_S estimates. (b) Estimations of the (frequency-independent) calibration filters between p and v_z over line 4 displayed as a function of receiver station number, using the optimization window in Figure 6. Note the correlation between the density estimate (a) and the calibration filter (b).

The condition imposed on the decomposition result is that there should be no direct wave or water bottom multiples in the upgoing normal stressfield below the bottom. The energy minimization is performed in a rectangular window over the direct wave in the τ, p domain (see Figure 5b, with the resulting optimization filter $\tilde{F}(p)$ on the right). It is not essential to make a tight fitting window as the direct wave has already much more energy compared to other events present in the window.

An important part in the adaptive decomposition scheme is the inversion of the filter $\tilde{F}(p)$ for the medium parameters just below the bottom. Without these medium parameters, the P- and S-wave decomposition in stage 5 cannot be accomplished. The decomposition operator $\varrho_1\beta_1/2q_{P,1}$ is fitted to the filter $\tilde{F}(p)$ by a least-squares optimization procedure, to obtain values for the density and P- and S-velocity. In this data example, the filters $\tilde{F}(p)$ better resembled the theoretical decomposition operators compared to the filter in Schalkwijk et al. (1999), which allowed for an automated inversion procedure.

An initial estimate of the medium parameters is obtained from the location on the p-axis of the singularities of $\tilde{F}(p)$ (giving $c_{P,1}$). Next, from the amplitude of $\tilde{F}(p)$ at $p=0$ (which is equal to half the P-wave impedance) an estimate of ϱ_1 is obtained. An initial estimate for $c_{S,1}$ is obtained by assuming a realistic velocity ratio ($c_{P,1}/c_{S,1}$). Once an initial estimate for the medium parameters has been obtained, the actual curve fitting is performed in the precritical ray-parameter domain, otherwise the large amplitudes of the singularities influence the curve fitting too much. However, inverting the filter for the medium parameters using only the precritical ray-parameter domain is not robust enough in the presence of noise. To obtain a more robust inversion, the following strategy was used:

1) First estimate c_P from the singularity location.
2) Keep c_P fixed, choose a realistic c_S, and estimate ϱ from a ray parameter interval around 0.
3) Keep c_P and ϱ fixed, and estimate c_S from a larger ray parameter interval, but not including the singularities.

The fluctuations in the inversion results for different receiver locations can give further information on the stability of the inversion procedure and the actual parameter changes over the line. The inversion results for line 4 (see Figure 2) are displayed in Figure 7. The c_P estimates remain quite constant over the line at a value around 1600 m/s. The ϱ estimates show more fluctuations from values in the order of 1500 kg/m^3 up to 2500 kg/m^3

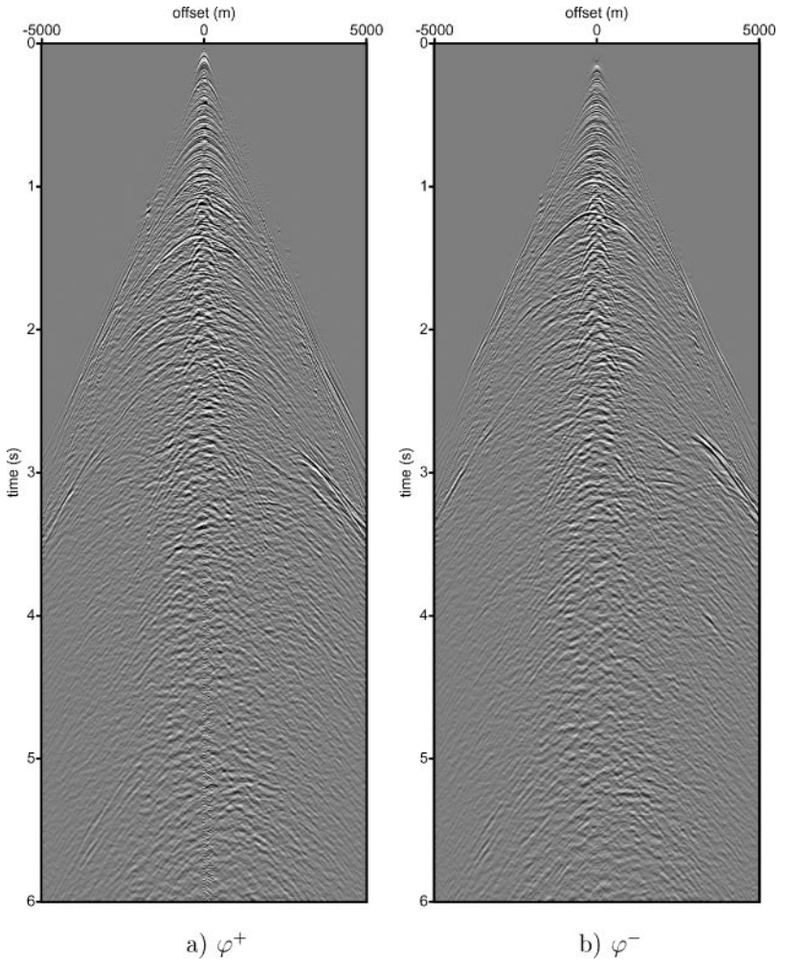

FIG. 8. Decomposition result of stage 5 applied to receiver gather 1321: (a) the downgoing P-potential just below the ocean bottom, (b) the upgoing P-potential.

and even two outliers above 2500 kg/m^3. The estimates for c_S lie around an average value of 300 m/s, with two inversion results giving an S-velocity of zero. From these results, it follows that the P-velocity is a robust estimate which varies little over the line. The S-velocity inversion easily becomes unstable in the presence of noise (estimates close to zero) because the S-velocity information is contained in the higher angles which is more affected by noise. Whether the fluctuations in the S-velocity that are displayed in Figure 7 correspond to the actual subsurface, therefore, cannot be determined. The fluctuations of the density estimates over the line also reflect the accuracy with which the calibration factor $A(\omega)$ has been determined. The inversion in stage 3 cannot distinguish between the density and the calibration factor, so it is assumed that this factor has been determined accurately in stage 2. However, for a shallow ocean bottom, all events are close together, and it is difficult to isolate a window with only primary energy, making it more difficult to find a reliable calibration factor. In Figure 7b, the fluctuations of the (scalar) calibration factor $A(\omega)$ over the line have been displayed below the inversion results (Figure 7a) to show the correlation between the calibration factor and the density.

Stage 4. Elastic decomposition into $\tau_{xz}^{\pm}$ just below the bottom

For the elastic decomposition below the bottom into downgoing and upgoing shear-stress fields, the pressure and horizontal velocity components are necessary, which makes it possible to resolve a calibration filter $B(\omega)$ between them. From the authors' experience, it appears that the vertical component calibration filter $A(\omega)$ cannot be used to calibrate the horizontal component as well. The equations for the downgoing and upgoing shear-stress fields follow by substituting the expressions for $\tilde{\mathbf{M}}_1^{\pm}$ and $\tilde{\mathbf{M}}_2^{\pm}$ into equation (6), yielding

$$-\tilde{\tau}_{xz}^{\pm} = \pm\frac{\gamma_1 p}{2q_{S,1}}\tilde{P} \pm B(\omega)\frac{\varrho_1\beta_1}{2q_{S,1}}\tilde{V}_x, \qquad (13)$$

where $q_{S,1}$ is the vertical S-wave slowness of the medium just below the bottom and γ_1 contains the P- and S-velocities. The decomposition operators, $(\gamma_1 p)/(2q_{S,1})$ and $(\varrho_1\beta_1)/(2q_{S,1})$, are calculated with the parameter estimates of the previous stage. Alternatively, an additional inversion for the S-velocity can take place in this stage. This procedure was adopted in Schalkwijk et al. (1999). The energy minimization is performed

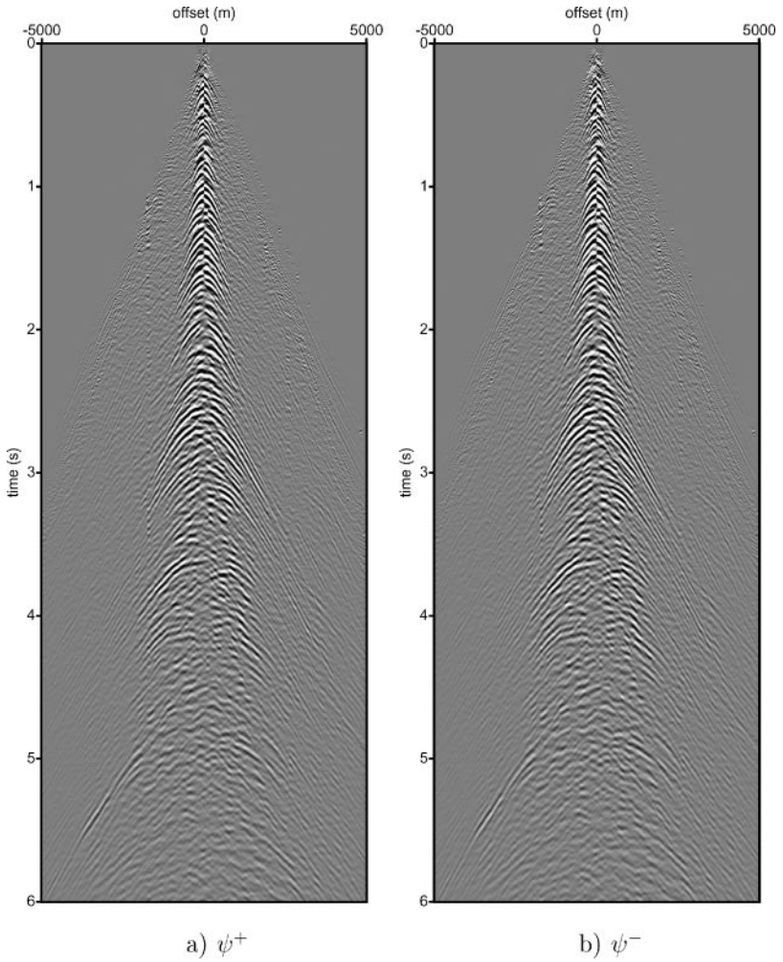

FIG. 9. Decomposition result of stage 5 applied to receiver gather 1321: (a) the downgoing S-potential just below the ocean-bottom, (b) the upgoing S-potential.

in a rectangular window over the direct wave in the τ, p domain (see Figure 5c, with the time domain version $b(t)$ of the resulting calibration filter $B(\omega)$ on the right), as both the downgoing and upgoing shear-stress fields should not contain the direct wave.

Stage 5. Elastic decomposition just below the bottom into P- and S-wave potentials

Substituting the expressions for $(\tilde{\mathbf{L}}_1^{\pm})^{-1}$ into equation (9), the equations for the downgoing and upgoing P- and S-wave potentials become

$$\tilde{\Phi}^{\pm} = \frac{c_{S,1}^2}{\beta_1}\left\{ \mp 2pq_{S,1}\tilde{\tau}_{xz}^{\pm} - \left(c_{S,1}^{-2} - 2p^2\right)\tilde{\tau}_{zz}^{\pm}\right\}, \quad (14)$$

$$\tilde{\Psi}^{\pm} = \frac{c_{S,1}^2}{\beta_1}\left\{\left(c_{S,1}^{-2} - 2p^2\right)\tilde{\tau}_{xz}^{\pm} \mp 2pq_{P,1}\tilde{\tau}_{zz}^{\pm}\right\}. \quad (15)$$

The decomposition result for one receiver gather (1321) is displayed in Figures 8 and 9 in the x, t domain. The medium parameters obtained from the inversion of the filter of stage 3, for this receiver gather, are $c_P = 1538$ m/s, $c_S = 128$ m/s, and $\varrho = 1129$ kg/m^3. As c_S is quite low, the decomposition mainly performs a separation of downgoing and upgoing wavefields and not so much of P- and S-waves, as the latter was already accomplished in the original geophone components due to the low S-velocity. A comparison of the prestack data with and without decomposition is displayed in Figures 10 and 11, where the vertical velocity component is displayed next to the upgoing P-waves and the horizontal velocity component next to the upgoing S-waves for receiver gather 1321.

The decomposition results over line 3, 4, and 5 (see Figure 2) have been combined to generate images of the subsurface. In Figures 12 and 13, the poststack time-migrated image of the subsurface obtained using the vertical velocity component can be compared with the image obtained from the upgoing P-waves after decomposition. The same can be done in Figures 14 and 15, where the horizontal velocity component (stacked) image and the image obtained from the upgoing S-waves after decomposition are displayed. The horizontal velocity and S-wave image results were made using the common-conversion-point method discussed by Tessmer and Behle (1988) and Harrison and Stewart (1993). In the time-migrated sections (Figures 12 and 13), a salt layer can be distinguished with the base of the salt roughly between 2.5 and 3 s. Especially in the P-wave image, a lot of multiple reflections are removed, compared to the

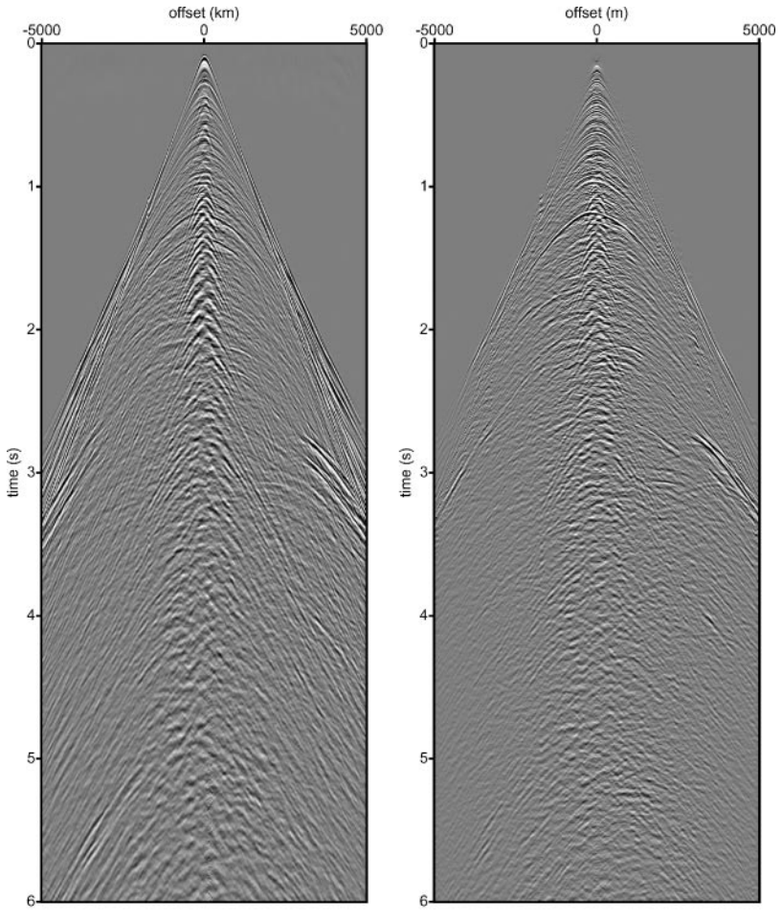

FIG. 10. Comparison of receiver gather 1321 before and after decomposition: (a) the vertical velocity component (after interpolation and deconvolution), (b) the upgoing P-potential just below the bottom.

vertical component image. Some attenuation of (multiple) energy can also be distinguished in the upgoing S-wave image, together with a better continuity of events compared to the image obtained from the horizontal inline velocity component (see, for example, at the arrows in Figures 14 and 15). In the image of the upgoing S-waves, the top of the salt can be seen between roughly 4 and 6 s. The base cannot be distinguished.

CONCLUSIONS

A brief review has been given of the decomposition theory, adapted for the case of multicomponent ocean-bottom data. The process separates the P- and S-waves from each other, as well as the downgoing and upgoing wavefields (thus removing most surface-related multiples from the upgoing wavefield). In practice, the decomposition equations are difficult to apply to field data because of unknown medium parameters, coupling effects, etc. Therefore, a five-stage adaptive decomposition procedure is used on field data. The adaptive scheme allows for some imperfections of the measurements (imperfect coupling of the geophones, energy leaking between the geophone components) and for unknown medium parameters just below the ocean bottom.

In this study the wavefield decomposition was tested on a field data set with a relatively shallow ocean bottom (≈120 m). Compared to ocean-bottom data acquired over deep water, this proved more challenging because of stronger interference between events. Deconvolution of the data, to remove the air bubble effect had to be done carefully, in order not to affect other interfering events. The determination of a window containing only primary events (stage 2 of the adaptive decomposition scheme) can be quite difficult for shallow data. When extending the decomposition to a full line of 2D ocean-bottom data by repeated application to all receiver gathers, the window determination in stage 2 is the most complicating factor. To avoid picking a different window for each gather, a combined window over different primary events is used. This does not give an equally good calibration result for all gathers in the line [alternatively, when the two-way traveltime operator in the water is well known, the calibration in stage 2 can be performed in any window outside the direct arrival (Soubaras, 1996; Lokshtanov, 2000), thus eliminating window determination problems for shallow data]. Although the decomposition theory requires application to common-shot gathers, it is in practice often only possible to use common-receiver gathers (due to statics, coupling, aperture limitations, etc.). Strictly speaking

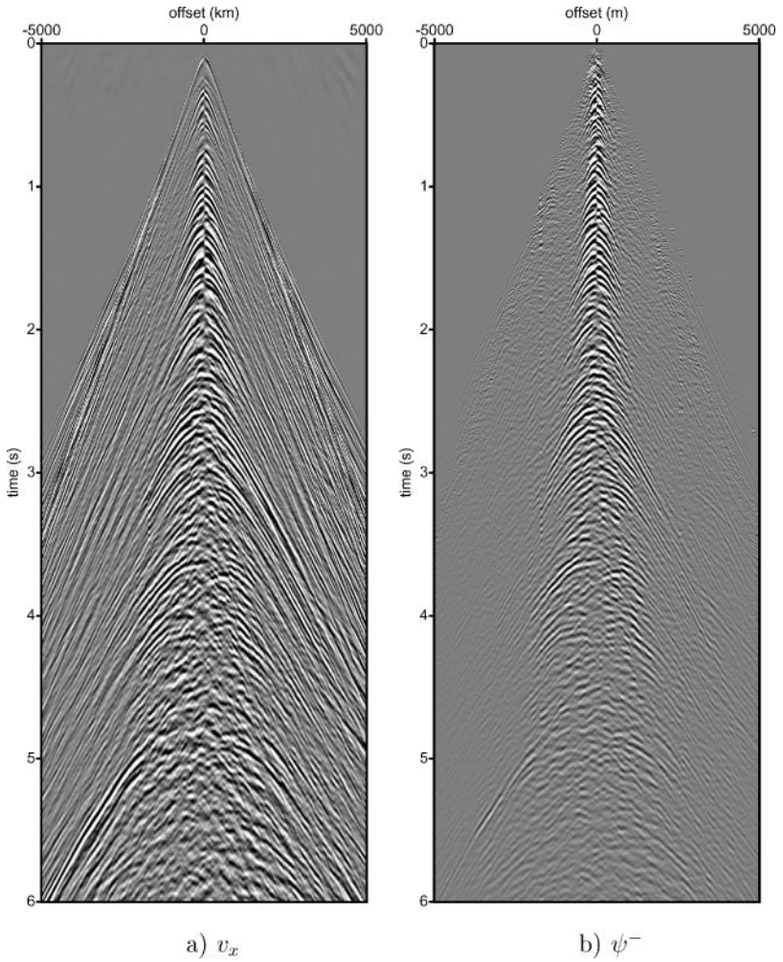

FIG. 11. Comparison of receiver gather 1321 before and after decomposition: (a) the horizontal inline velocity component (after interpolation and deconvolution), (b) the upgoing S-potential just below the bottom.

it is only correct to substitute common-shot gathers by common-receiver gathers when the medium is laterally invariant. Experiences with field data show that it is still allowed to do so with mild lateral medium variations present. Note that this assumption only affects the amplitude behavior of the events, not the traveltime.

The optimal filters obtained in stage 3 quite nicely resemble the theoretical decomposition operators. For field data, the inversion procedure was stabilized by fixing the ray parameter of the critical angle. From the several inversion results obtained along the line, the sensitivity of the medium parameter inversion could be investigated. The P-velocity is well determined by the inversion. A realistic density estimate for field data was not always possible because the density is interrelated with the coupling factor of the vertical velocity component. The reliability of the density estimate, therefore, depends on how well the coupling factor could be estimated (stage 2 of the adaptive decomposition scheme). Conversely, if the density estimates are way off the mark, this is an indication that the coupling determination in stage 2 was not accurate enough. This is demonstrated by the density estimates in the field data example. The S-velocity estimate is difficult to obtain from the filter of stage 3 because it is very sensitive to the signal-to-noise ratio and depends on high(er) angles. Moreover, it is also sensitive to (small) errors in the P-velocity estimate. The inversion was stabilized to obtain reasonable S-velocity values over the line.

To evaluate the benefit of the wavefield decomposition on the image quality of the subsurface, a poststack time migration was performed on the measured data components as well as on the decomposed upgoing P- and S-waves. The effect of multiple attenuation/removal is evident after wavefield decomposition. To evaluate the effect of P- and S-wave separation kinematically is more difficult. Nonetheless, the upgoing S-wave image displays a generally better continuity of events, along with some attenuation of multiple energy when compared to the image obtained by simply using the horizontal velocity component. It must be realized, however, that by the stacking procedure itself,

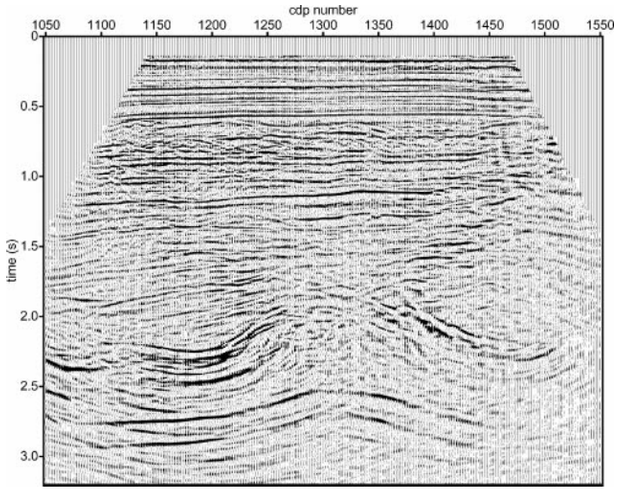

FIG. 12. Poststack time-migrated section of the vertical velocity component.

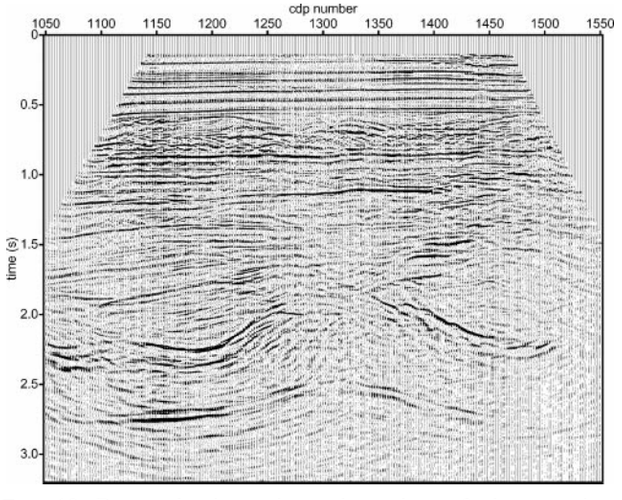

FIG. 13. Poststack time-migrated section of the upgoing P-potential just below the ocean bottom.

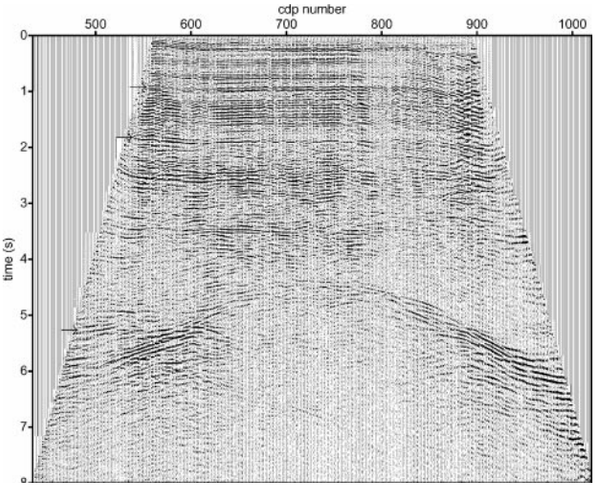

FIG. 14. Common-conversion-point stacked section of the horizontal inline velocity component v_x, using $c_P/c_S = 3.5$. Arrows mark some events that have been improved after decomposition.

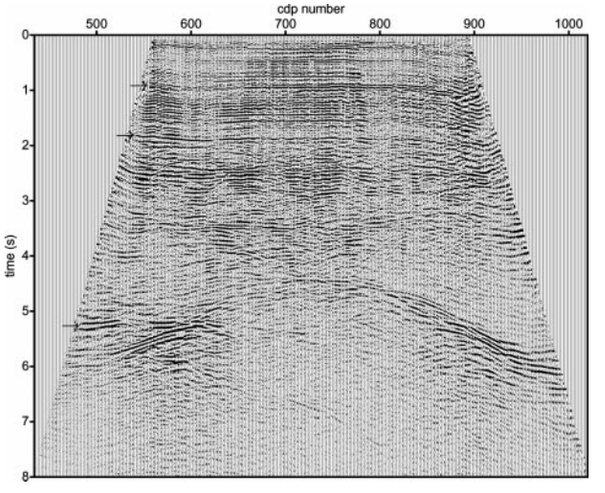

FIG. 15. Common-conversion-point stacked section of the upgoing S-potential just below the ocean bottom, using $c_P/c_S = 3.5$. Arrows mark some events that have been improved after decomposition.

some effects of the wavefield decomposition are concealed, for example angle dependent reflectivity effects.

ACKNOWLEDGMENTS

The authors thank BP for permission to use the data set.

REFERENCES

Aki, K., and Richards, P. G., 1980, Quantitative seismology: Freeman.
Frasier, C. W., 1970, Discrete time solution of plane P-SV waves in a plane layered medium: Geophysics, **35**, 197–219.
Harrison, M. P., and Stewart, R. R., 1993, Poststack migration of P-SV seismic data: Geophysics, **58**, 1127–1135.
Kennett, B. L. N., 1983, Seismic wave propagation in stratified media: Cambridge University Press.
Lokshtanov, D., 2000, Suppression of free-surface effects from multicomponent sea-floor data: 62th Mtg., Eur. Assn. Expl. Geophys., Extended Abstracts, L-52.
Schalkwijk, K., 2001, Decomposition of multi-component ocean-bottom data into p- and s-waves: Ph.D. diss., Delft University of Technology.
Schalkwijk, K. M., Wapenaar, C. P. A., and Verschuur, D. J., 1999, Application of two-step decomposition to multicomponent ocean-bottom data: Theory and case study: J. S. Expl., **8**, 261–278.
Soubaras, R., 1996, Ocean-bottom hydrophone and geophone processing: 66th Ann. Internat. Mtg. Soc. Expl. Geophys., Expanded Abstracts, 24–27.
Tessmer, G., and Behle, A., 1988, Common reflection point data-stacking technique for converted waves: Geophys. Prosp., **36**, 671–688.
Ursin, B., 1983, Review of elastic and electromagnetic wave propagation in horizontally layered media: Geophysics, **48**, 1063–1081.
Wapenaar, C. P. A., Verschuur, D. J., and Herrmann, P., 1992, Amplitude preprocessing of single and multicomponent seismic data: Geophysics, **57**, 1178–1188.